Materials Transactions, Vol. 60, No. 8 (2019) pp. 1442 to 1449
Special Issue on Recent Advances in Indentation Technique

Direct *In Situ* Observation of Deformation Modes in Wedge Indentation of Metals

Anirudh Udupa[1], Narayan Sundaram[2], Tatsuya Sugihara[3] and Srinivasan Chandrasekar[1,*]

[1]*Center for Materials Processing and Tribology, West Lafayette, IN 47907, USA*
[2]*Department of Civil Engineering, Indian Institute of Science, Bengaluru, 560012, India*
[3]*Department of Mechanical Engineering, Osaka University, Suita 565-0871, Japan*

We study deformation patterns in wedge indentation of annealed metals (e.g., copper) using high-resolution, *in situ* imaging and image correlation. Based on attributes of the deformation such as velocity fields, grid distortion and strain distributions, we discriminate between two modes of deformation — a cutting mode with narrow-angle (sharp) wedges, e.g., apex angle of 30°, and a radial-compression mode with wide-angle (blunt) wedges, e.g. apex angle of 120°. The cutting mode is characterized by significant material flow parallel to the wedge face; and a thin region of very high strain (∼3), that is located immediately adjacent to the indenter face (wall-layer), and arises from friction-induced deformation. The radial-compression mode is distinguished by material flow normal to and away from the indenter face, with negligible velocity component parallel to the indenter face. The corresponding strain field is one of bulk deformation, with the highly-strained region (strain ∼1) being of semicircular shape that extends from near the edge of indenter contact at the specimen surface, to well below the indenter tip. The observations show that indenter wall friction is likely to have a major influence on the deformation field only with narrow-angle indenters.

Based on the observations of material flow, a suggestion is made (and validated) as to how the challenges faced in computational modeling of narrow-angle wedge indentation can be overcome. Implications for use of narrow-angle wedge indentation to study tribology of metalworking contacts, and ductile failure and damage in metals, are briefly discussed. [doi:10.2320/matertrans.MD201906]

(Received January 7, 2019; Accepted May 9, 2019; Published July 25, 2019)

Keywords: *metals, indentation, high-speed imaging, deformation, plasticity, cutting*

1. Introduction

Quasi-static indentation by wedges (pyramids) and similar sharp indenters, widely used in hardness testing of metals and for assessment of their mechanical behavior,[1–3] has a rich history of experimental and theoretical investigation.[4–10] Since the indentation response is closely related to the deformation field, the nature of deformation patterns under wedge, cone and spherical indentations has been of long-standing interest. The deformation patterns have been studied experimentally, most notably, by analyzing changes in shape of an inscribed rectangular grid,[5,7] using microstructural features as markers,[11,12] and assessment of changes in the material's hardness in the indentation zone.[2,12] These techniques for studying the deformation are, however, limited in one or more of the following aspects: spatial resolution, temporal resolution, field of view and quantitative assessment of deformation. More recently, electron microscopy (EBSD) has been used to determine certain attributes of the deformation such as lattice rotations in indentation of single crystals[13] and dislocation mechanics;[14] however, these techniques offer little scope for studying plastic strain and other quantitative measures of deformation associated with the indentation.

The nature of the contact conditions at the indenter-material interface also suggests opportunities for utilizing indentation to study friction phenomena of relevance to metal forming and cutting processes. These contact conditions are characterized by intimate contact and high normal contact pressures, the latter being equal to the material hardness. Furthermore, the real area of contact between the indenter and the metal under conditions typical of hardness testing is equal to or a large fraction of the geometric (apparent) area of contact. Such conditions are very similar to those prevailing at die and tool interfaces in deformation processing (e.g., rolling, extrusion, piercing, punching) and machining processes.[15]

Both hardness testing and application of indentation to study friction in processing can greatly benefit if improved methods are available to characterize the deformation field attributes under an indenter at high spatial and temporal resolution. This characterization includes qualitative analysis of types of deformation patterns, and quantitative analysis of deformation parameters such as material displacement and velocity fields, strain and strain rate, and indenter wall slip.

In this study, we demonstrate an experimental method for carrying out precisely this type of deformation characterization in indentation of metals. In particular, the method is tuned to study the dependence of flow patterns on indenter angle. It combines direct *in situ* imaging of material flow with an image correlation technique, Particle Image Velocimetry (PIV), to map deformation patterns at high resolution. The method is illustrated by its application to indentation of annealed oxygen-free high-conductivity (OFHC) copper by wedges of different apex angles ($2\alpha =$ 30°, 90° and 120°). We show, among other things, a clear transition in the mode of deformation from one resembling radial compression at larger apex angles (e.g., 120°) to a "cutting" mode characterized by transverse displacement of material away from the indenter axis at smaller apex angles (e.g., 30°), confirming preliminary results discussed in Ref. 16). Quantitative mapping of velocity and strain fields in and around the indentation is presented. The viability of studying friction using narrow-angle wedge indentation is highlighted. Lastly, based on the observations, a model for simulating material deformation in narrow-angle wedge indentation, a hitherto unresolved problem, is outlined. The deformation characterization is quite general and applicable to metals; it builds on prior work on analysis of large-strain deformation in indentation, cutting and forming processes.[16–19]

*Corresponding author, E-mail: chandy@purdue.edu

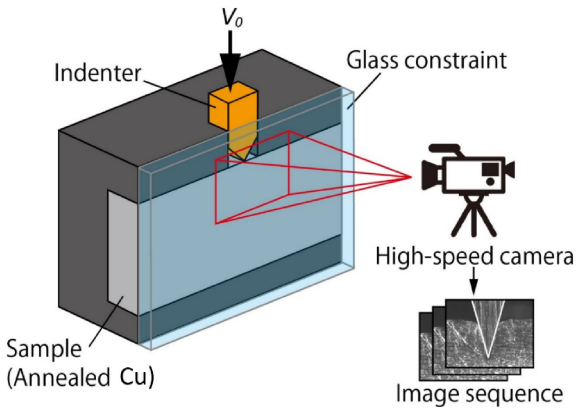

Fig. 1 Schematic of experimental setup for *in-situ* imaging of indentation. The high-speed image sequence is analyzed to obtain quantitative flow field information at high resolution.

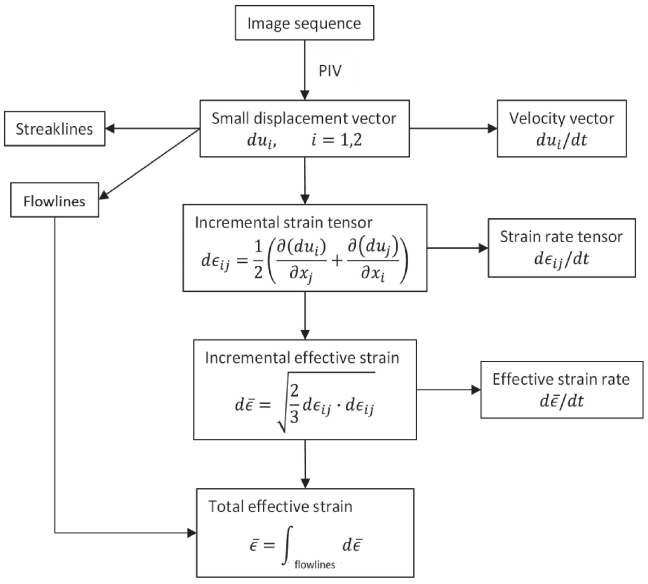

Fig. 2 Flow chart describing computation of flow and deformation parameters by PIV.

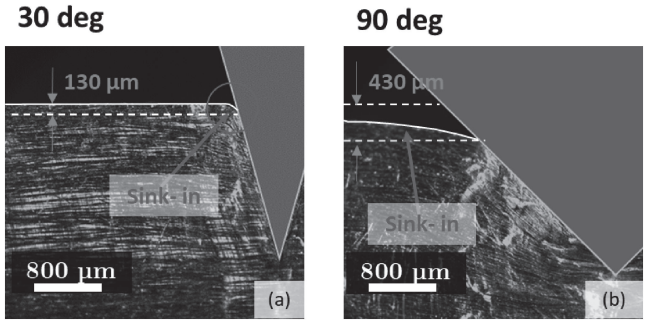

Fig. 3 Typical images of the deformation region acquired by the high-speed camera in indentation with (a) 30° and (b) 90° wedges. The images also show sinking-in near the edge of indenter-workpiece contact at the specimen surface. This is typical of indentation of annealed metals. Both indenters penetrated the material by ~2 mm.

2. Experimental

Figure 1 shows a schematic of the experimental configuration used for the quasi-static indentation, and direct *in situ* observation of the deformation in the indentation zone, including in the vicinity of the indenter wall. OFHC Cu specimens for indentation (63.5 mm × 25.4 mm × 9.5 mm) were annealed at 950°C for 3 hours. The annealed specimens, hardness 68 HV, were then indented at 0.1 mm/s using high-speed steel wedges of apex angles (2α) of 30°, 90° and 120°. The indentation depth was typically in the range of 1.5 to 2 mm. The indentations were done in a Universal Test Machine (MTS QTest/50LP) with the indenter attached to the machine cross-head, and under displacement-control mode at a set cross-head speed of 0.1 mm/s. The load was measured as a function of cross-head displacement; this data is reported as load-penetration curves. Prior to the experiments, the indenter faces were prepared by grinding to a smooth finish and with a tip radius of <5 µm. Since this radius is very much smaller than the penetration depth (1.5 to 2 mm), the indenter could be considered as ideally sharp. The 3-D topography of the indenter surface in contact with the metal was obtained by optical profilometry; the S_a value for this surface was ~0.4 µm, quite typical of smoothly ground surfaces. The indentations were done dry, without application of any lubricant.

A transparent glass block was clamped against the specimen to restrict out-of-plane flow and ensure two-dimensional (plane strain) deformation. During indentation, the side of the Cu specimen in the indenter vicinity and the indenter wall region were imaged through the glass at 20 fps using a CCD camera–optical microscope assembly and a 5X objective lens. This enabled an area of ~5.6 × 4.5 mm in the indenter vicinity to be imaged with spatial resolution of 2.8 µm/pixel. The use of the glass block also facilitated focusing on to the specimen/indenter sides during the imaging. From the high-speed image sequences, displacement and velocity fields of material flow were obtained by image correlation using particle image velocimetry (PIV).[17,20] Deformation parameters such as strain rate tensor, effective (von Mises) strain rate and effective strain were computed as described in Fig. 2;[17,18] it is these values that are reported unless otherwise stated. The image correlation and deformation computation were implemented using MATLAB. Additionally, material flow was visualized using distortion of (virtual) grids and via flow lines.[17,21] In this manner, the deformation fields could be studied as a function of indenter angle and depth of penetration.

3. Results

Figures 3(a) and 3(b) show sample images (frames) of the indentation region, as recorded by the high-speed camera, for the 30° and 90° wedge, respectively. The indenter (cross-head) penetration depth in both cases was 2 mm. Thus, the indenter tip in Fig. 3 is located ~2 mm from the specimen surface. The topmost line in each figure shows the initial location of the Cu surface, that is prior to indenter loading; while the lower dotted line is level with the edge of indenter-specimen contact. It is seen from Fig. 3(b) ($2\alpha = 90°$) that the surface of the Cu immediately adjacent to the indenter has "sunk in" with respect to its initial location. The extent of this sinking-in is about 430 µm (distance between dotted lines), which includes also any local bending of the sample surface.

This sinking-in is much less pronounced, ~130 μm, with the narrow wedge ($2\alpha = 30°$) in Fig. 3(a). The sinking-in observed is typical of indentation of annealed metals.[1,2)]

From analysis of image sequences, each frame of which is similar to those seen in Fig. 3, the velocity and displacement fields were computed using PIV analysis. Figures 4(a), 4(b) and 4(c) show the velocity fields in the indentation zone for $2\alpha = 30°$, 90° and 120°, respectively. The color map (background) in these figures gives the material velocity magnitude, as measured with respect to the indenter (i.e., velocity relative to the indenter). The overlaid quiver plot gives the direction and magnitude of the local velocity, with the arrow length being proportional to the velocity magnitude. Again, the velocities are plotted with respect to the indenter velocity. Henceforth, unless stated otherwise, the term velocity will refer to this relative velocity.

3.1 Material flow

The velocity fields in Fig. 4 are strikingly different. Firstly, it is seen that the velocity magnitude decreases with increasing indenter angle. This is for the fixed indenter speed. Secondly, and perhaps most importantly for understanding the deformation patterns, the direction of material motion is very different especially for $2\alpha = 30°$ and 120°. In the $2\alpha = 30°$ case (Fig. 4(a)), the material is seen to flow tangential to (and past) the tool face with a velocity of 0.09–0.1 mm/sec, though with some retardation close to the tool face as a result of friction. The retardation is obvious from the velocity quiver. It is also clear from the quiver plot that if we consider two points initially located very close to one another under the approaching indenter tip, but on opposite sides of the symmetry axis of the indenter, they will, after the indentation, be located (displaced) far away from each other—that is analogous to as if the material were "cut" along the symmetry axis by the indenter. Hence, this deformation pattern characterized by large velocities tangential to the indenter face may be identified with the cutting mode of deformation initially outlined by Hill.[5)] The material flow near the indenter tip in Fig. 4(a) resembles that seen near the edge of a tool (tip) in cutting of metals by sharp wedges,[22,23)] or even that seen in "splitting" of wood, thus reinforcing assignment of the term "cutting" to this mode of deformation. It is also reminiscent of fluid flow past a sharp obstacle. The PIV analysis, in its current form, is unable to resolve whether material separation is occurring just ahead of the indenter tip, or whether a very thin layer of the Cu material immediately adjoining the indenter face has been stretched to very large strains. Both of these types of deformation (representing two extremes in deformation modes) can explain the observed large separation between points that were initially located very close to each other, but on opposite sides of the indenter symmetry axis. Elsewhere, over most of the indentation region and away from the indenter face, the material velocity is close to 0.1 mm/sec (the indentation speed).

In contrast to Fig. 4(a), the velocity field in Fig. 4(c) ($2\alpha = 120°$) is characterized by negligible material motion tangential to the indenter face. Instead, it can be deduced from the figure that material flow in and around the contact is primarily normal to the indenter face. Furthermore, since the velocity is essentially zero over a large, approximately semi-circular region (blue color region, Fig. 4(c)) surrounding the indenter, it means that the material in this region is essentially moving with the indenter. In this sense, it acts as an extension of the indenter. Note however that with increasing indenter penetration the size of the "zero velocity" region grows. This deformation pattern, characterized by a large region of material flow occurring normal to the indenter face may be identified with the radial compression mode identified by Mulhearn *et al.*[7,24)] In this mode of flow, points located close to one another under the indenter tip, but on either side of the indenter symmetry axis, are not displaced that far apart after the indentation, as in the cutting mode case.

The deformation pattern in Fig. 4(b) ($2\alpha = 90°$) is intermediate between that of Figs. 4(a) and 4(c), though closer to the radial compression mode of Fig. 4(c), since there is a small, though sizable zone, of zero material velocity underneath the indenter. Furthermore, the velocity quivers indicate that the material flow tangential to the tool face is also not significant for this $2\alpha = 90°$.

This classification of the deformation into radial-compression and cutting modes using the velocity fields is

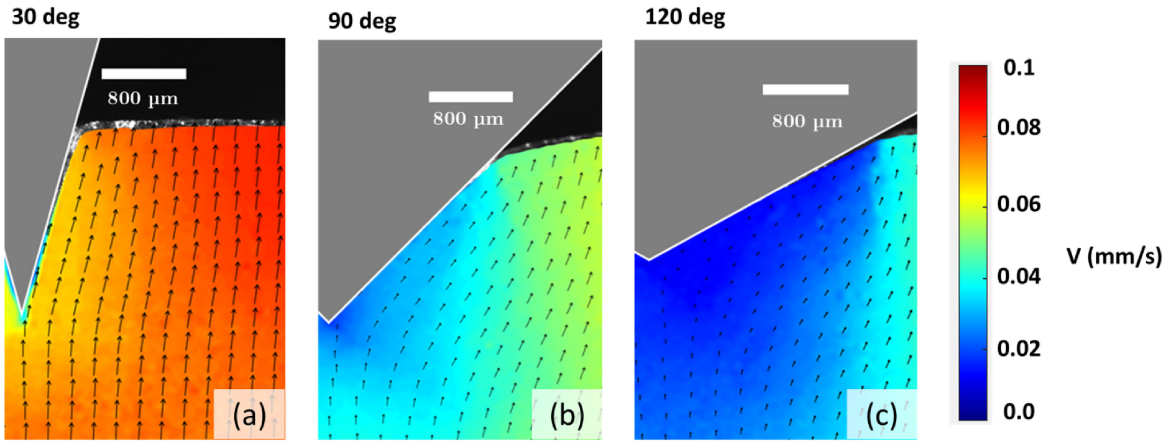

Fig. 4 Velocity fields in indentation with (a) 30°, (b) 90° and (c) 120° wedges. The color maps show the magnitude of material velocity with respect to the indenter obtained by PIV. The overlaid quiver plot indicates both the direction and magnitude of the velocity. The material flow is tangential to the indenter face in 30° case, whereas it is essentially normal to the indenter face in the 90° and 120° case.

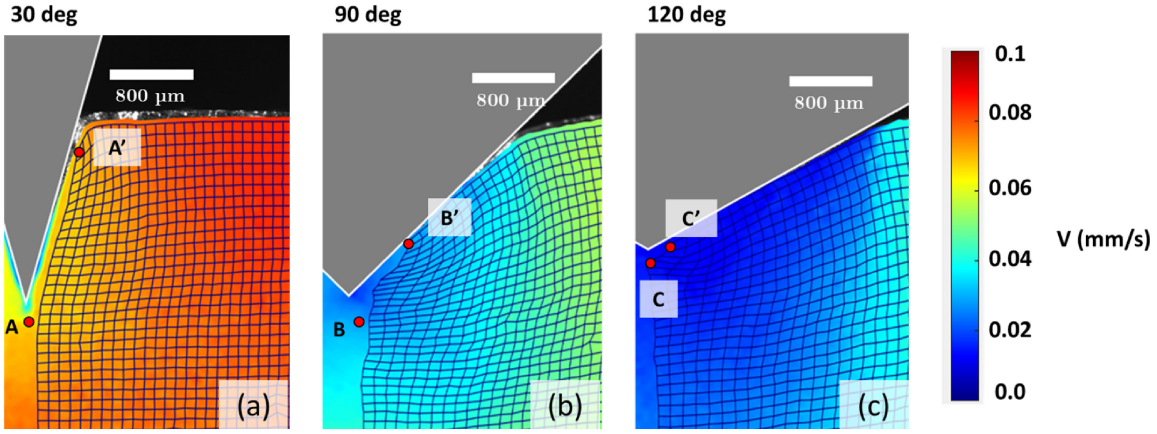

Fig. 5 Grid deformation and background velocity fields for indentation with (a) 30°, (b) 90° and (c) 120° wedges. Prior to the indentation, each grid was rectangular. A, B and C indicate the positions of select points on the grid that were located initially close to the specimen surface and just below the indenter tip. A′, B′ and C′ are the locations of these points after the indentation.

reinforced by analysis of grid distortion as in visioplasticity. Figures 5(a)–5(c) ($2\alpha = 30°$, 90°, 120°, respectively) show pictures of initially rectangular (virtual) grids, embossed in the material, after they have undergone deformation due to the indentation. These figures parallel Figs. 4(a)–4(c). The background color map again gives the local material velocities with respect to the indenter. Certain features (attributes) of this grid deformation, all closely related, are worth highlighting in the context of classifying the deformation into cutting and radial-compression modes.

Firstly, the grid patterns show that very little deformation occurs below the indenter tip region for $2\alpha = 30°$ (Fig. 5(a)) but considerable deformation for the case of $2\alpha = 120°$ (Fig. 5(c)). This suggests that the extent of sub-indenter tip region deformation provides a good signature for discriminating between the cutting and radial-compression modes. The $2\alpha = 90°$ case (Fig. 5(b)) is intermediate in terms of the deformation, but much closer to the $2\alpha = 120°$ radial-compression grid pattern. Secondly, consider points such as A, B and C (Fig. 5) located initially just within the Cu specimen subsurface and close to the approaching indenter tip. The locations of these points, after the indentation, are A′, B′ and C′, respectively. In the $2\alpha = 30°$ case, the point A has thus moved from its initial location just underneath the indenter to a final location very close to the free surface. In the 90° wedge case, the analogous point (point B) moves from just underneath the indenter to roughly a third of the way up the indenter face to location B′, while in the 120° wedge case, the same point (point C here) is displaced by only a small amount parallel to the indenter face to C′. The latter is consistent with a well-developed radial-compression type of flow prevailing. Thus, the extent of displacement of material points (material elements), that are initially located close to the indenter tip (e.g., A, B, C), in the direction parallel to the indenter face, provides a quantitative measure for discriminating between the cutting and radial-compression flow modes — the larger this displacement, the more dominant the cutting mode of deformation.

A third attribute of the deformation pattern is to be found in the angle that the (initially) vertical grid lines make with the indenter face after the indentation. In the $2\alpha = 30°$ case, these lines are essentially parallel to the indenter face, as in Fig. 5(a), and consistent with the cutting mode. However, with the 120° wedge, these lines are nearly normal to the indenter face (Fig. 5(c)) and consistent with the radial flow mode. In the 90° case, the pattern is somewhat intermediate (Fig. 5(b)), though much closer to the 120° case, with the initially vertical lines meeting the wedge face almost perpendicularly. Hence the intersection of the grid lines with the indenter face provides another discriminator of the deformation mode. It should be noted however that these features of the deformation are not all independent attributes but a direct consequence of the specific velocity field of material flow.

3.2 Plastic strain field

Figures 6(a)–6(c) show the plastic strain distributions (von Mises effective strain) for $2\alpha = 30°$, 90° and 120°, as estimated by the PIV analysis. Two zones of high strain can be seen in these figures. One of these zones (zone 1) is a thin layer of very high strain (>1.5) that is immediately adjacent to the indenter face (indenter-Cu contact), while the second one (zone 2) is a much larger pocket of somewhat lower strain (~0.8 and above, high-strain zone) that is outlined by red dotted lines in the figures. It is important to distinguish between these two zones as they have different origins. Firstly, considering zone 2: In the $2\alpha = 30°$ case (Fig. 6(a)), this pocket, relatively small, is located quite close to the Cu specimen surface and far away from the indenter tip. In contrast, with the $2\alpha = 120°$ wedge (Fig. 6(c)), this pocket is quite large and of semi-circular shape, extending all around the indenter from the specimen surface (near edge of indenter contact) to ~800 µm below the indenter tip. This type of strain distribution is a consequence of the radial-compression flow mode, and exhibits the underlying symmetry of this flow mode. In the $2\alpha = 90°$ case (Fig. 6(b)), the pocket while large is split into two "whisker-shaped" regions, each of which extend from the indenter tip to the free surface (at the edge of the indenter contact) and reflecting the 2-fold symmetry of the wedge. The pocket shape here is almost as if the semi-circular zone 2 of Fig. 6(b) has split (bifurcated)

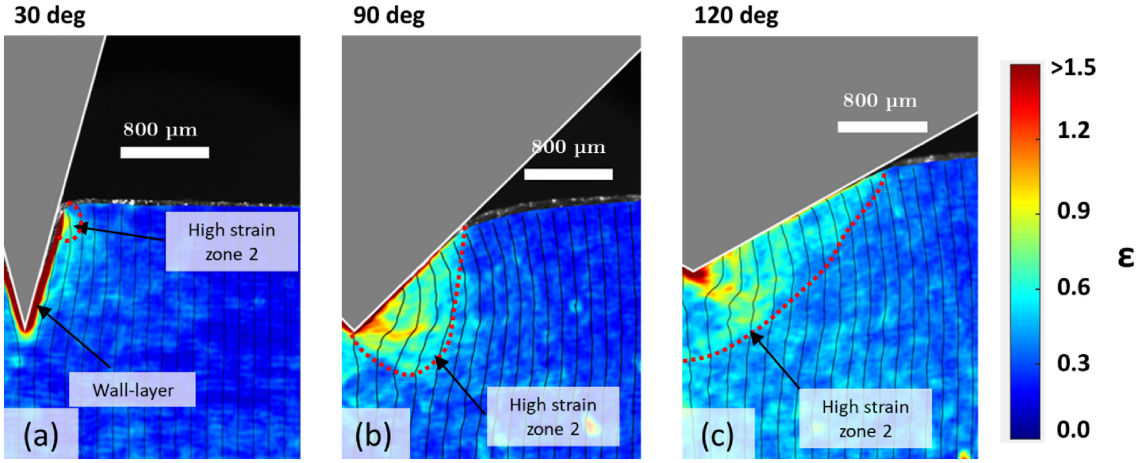

Fig. 6 Plastic strain distributions obtained from experiment for indentation with (a) 30°, (b) 90° and (c) 120° wedges. The red-dotted lines indicate boundary of high-strain zones (>0.8).

into two regions. This is consistent with a transition developing between the radial-compression and cutting modes. At angles somewhat below 90°, a more cutting type of flow mode may be expected to occur. Zone 2 is a consequence of the bulk deformation occurring in the Cu due to the indentation loading.

Secondly, turning to the very high strain layer adjoining the indenter face (zone 1): this zone is seen to be most pronounced with the 30° wedge, with strain >3 and of ~100 µm thickness (wall layer), see Fig. 6(a). This zone of very high strain has its origin in friction-induced deformation, due to the material flow parallel to the indenter face (wall) and the retardation of flow observed in this wall region. However, when material flow parallel to the indenter face is minimal, with negligible slip between the indenter and the Cu specimen, then this wall-layer of very high strain disappears, as with the $2\alpha = 120°$ wedge (Fig. 6(c)). The zone 1 wall layer does occur with the 90° wedge (Fig. 6(b)), but it is of much smaller thickness, ~30 µm, compared to the layer observed with the narrow-angle, 30° wedge. For reference, the deformed, initially vertical lines of the grid are shown in the background in Fig. 6; their orientations with respect to the indenter face are as discussed earlier.

The differences in the strain-distribution with different wedge angles is also reflected in the indenter load. Figure 7 shows the indenter load as a function of the penetration depth (cross-head displacement) for the three wedge angles, as measured by the load cell on the Universal Test Machine. The indentation load required for a given depth of penetration is seen to increase with the wedge angle. This is consistent with the fact that the size of zone 2 increases with α (see Fig. 6). A larger zone 2 indicates that a greater volume of material is strained, and hence more energy is consumed in penetration of the wedge.

From these observations it would appear that if one were interested in studying friction and friction-induced deformation under conditions of severe contact stresses, then the narrow-angle indenter loading is the preferred configuration ($2\alpha = 30°$ or smaller). It has recently been established that the wall layer of very high strain (zone 1), seen with narrow wedges, exhibits characteristics typical of a Bingham-fluid like boundary layer.[25)]

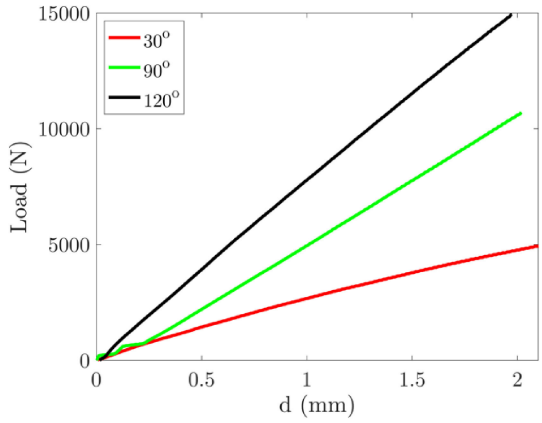

Fig. 7 Variation of indentation load with penetration depth (cross-head displacement) for different wedge angles.

4. Discussion

Our *in situ* observations of the indentation zone in deep indentation (~2 mm indenter penetration) coupled with image analysis of high-speed image sequences of the indentation process have provided a characterization of the two principal types of deformation patterns — cutting mode with narrow-angle indenters, and the radial-compression mode with wide-angle indenters — and of select quantitative attributes of these patterns. In particular, it has been demonstrated that different signatures of the deformation such as velocity of material flow, grid deformation and strain fields can be used to clearly and, potentially, quantitatively differentiate between these modes. The cutting mode is characterized by material flow parallel to the indenter face, a relatively small level of deformation in the sub-tip indenter region, a very highly-strained (>3) indenter-wall layer of ~100 µm thickness, and flow retardation along the indenter face (Figs. 4(a), 5(a) and 6(a), $2\alpha = 30°$). Another key feature of this deformation mode is that points, initially, just straddling the indenter symmetry axis, but located very close to one another in the indenter-tip region, are displaced and located far apart from each other after the indentation is complete (Fig. 5(a)).

In contrast, the radial-compression mode observed with a wide-angle indenter ($2\alpha = 120°$) is distinguished by large-scale material flow normal to the indenter face, negligible material flow parallel to the indenter face, and moderately strained zone (strain ~0.8) that extends deep into the indentation hinterland and radially from the indenter (bulk deformation), see Figs. 4(c), 5(c) and 6(c). This bulk deformation zone is of semi-circular shape and is quite large, extending as much as 800 μm from the indenter tip along the symmetry axis. Furthermore, initially vertical grid lines intersect the indenter face at near right-angles (i.e., normally) after the indentation is complete consistent with the radial flow of metal from the indenter. Since the wall-layer of very high strain adjoining the indenter face is negligibly small with the radial-compression mode, and is concomitant with minimal material slippage with respect to the indenter face, friction effects can be expected to play only a secondary role in indentation with wide-angle wedges. This is consistent with what has been inferred and/or assumed in hardness testing with pyramidal indenters, based on both experimental observations, and analyses such as using slip-line fields.[1,2)]

The thin, highly-strained, indenter wall layer (Fig. 6(a)) associated with the cutting mode of deformation ($2\alpha = 30°$) is a consequence of friction-induced deformation. This is evident from the nature of material flow and retardation of this flow in the vicinity of the indenter face. Hence, a detailed study of the characteristics of this highly-strained wall layer, e.g., amount of slippage at the indenter face, velocity gradient with distance from the wall, "boundary layer" structure, may be expected to provide fundamental insights into friction phenomena operative under conditions of high normal and shear stresses. This has been a little-explored area, but with considerable interest to metal forming and cutting processes.[15,22)] The narrow-angle indentation configuration, coupled with the direct observational approach, thus offers a framework in which tribology of metals under severe contact conditions can be explored systematically and quantitatively. A step in this regard has already been taken with initial results presented in a companion study.[25)]

4.1 Modeling of narrow-angle indentation

The direct observations and analysis of flow fields presented in this study have implications also for computational modeling and simulation of indentation by narrow-angle indenters. We shall here, without entering into detailed review of prior work on modeling of indentations, briefly discuss how the present experimental observations can facilitate accurate modeling of narrow-angle wedge indentation.

While finite element (FE) analysis of indentation by spheres,[26)] wide-angle cones,[27)] pyramids,[28)] and wide-angle wedges[29,30)] is fairly 'routine', the simulation of narrow ($2\alpha < 60°$) wedge indentation has posed serious problems. Attempts to address this in modeling are fairly recent: the most notable effort in this regard has been that of Hazell[31)] who considered indentation of soil by narrow cones, where similar computational difficulties, as with metals, occur. The procedure adopted in Ref. 31) was to add a protruding "knife edge" to the indenter tip, effectively pre-separating the material.

Our observations provide insight into why narrow-angle wedge indentation has been difficult to model and possible approaches to overcoming the challenges. The difficulty is most likely due to occurrence of the cutting mode of deformation at small apex angles. In this mode, as already-discussed, the nature of the flow leads to large separations between material points that were initially located close to one another under the indenter-tip, but slightly off the indenter symmetry axis (Fig. 5(a)). In fact, such material points can move considerable distances up the indenter face, and even to the specimen free surface itself, as seen in Fig. 5(a). Such a flow cannot be simply replicated in a conventional Lagrangian FE framework if one strictly enforces the displacement boundary condition (bc) along the symmetry axis (see schematic in Fig. 8(a)), namely

$$u_x = 0 \quad y < 0$$

For then, one vertical side of a hypothetical square, subsurface element would be anchored to the symmetry axis, while its adjacent sides would be stretched indefinitely. The

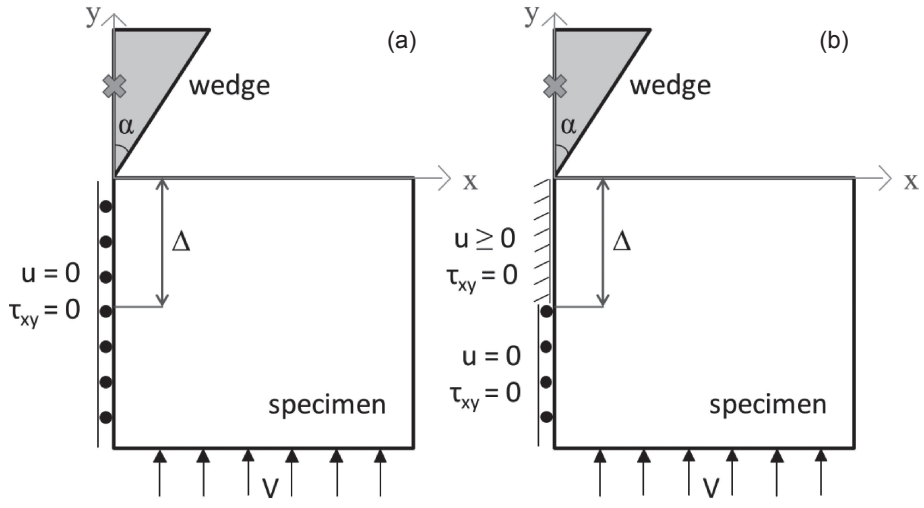

Fig. 8 Schematic of (a) 'strong' and (b) 'weak' symmetry boundary conditions in wedge indentation. One-way lateral displacements $u \geq 0$ are permitted along the symmetry line in case (b).

above bc may be termed as the "strong boundary condition" and is what has been typically used in modeling of wide-angle wedge and cone indentation.

Physically, the large separation (displacement) of just off-axis points, seen in the experiments with the $2\alpha = 30°$, wedge, can be envisaged to occur in one of two ways: either by failure of the material located along the indenter axis just ahead of the indenter (minimal cohesion in FE parlance) or by very large stretching of the material immediately adjoining the indenter faces (maximal cohesion), i.e., in the indenter-wall region (Of course, there could be intermediate situations comprised of both stretching followed by failure occurring).

In the former case, the one involving material failure with minimal cohesion, a 'weak' form of the boundary condition (see Fig. 8(b), Δ = indenter penetration),

$$u_x \geq 0 \quad -\Delta \leq y < 0$$
$$u_x = 0 \qquad y \leq -\Delta$$

can support such motion. Here, u_x is the displacement perpendicular to the indentation (y) axis and Δ is the depth of indentation. Note that the weak bc includes the strong bc as a special case, and its use effectively treats the symmetry line as an interface for material separation. Physically, the weak bc means that material separation can occur transverse to the symmetry axis (analogous to a crack), but no material inter-penetration can occur along this axis. With this modification, the simulation of indentation by a narrow wedge can be carried out in a conventional Lagrangian FE framework, as first proposed in our earlier work.[16)]

Figure 9(a), (b) and (c) shows deformed grids and strain distributions derived from FE simulation of indentation with $2\alpha = 30°$, 90° and 120° wedges, respectively, for the weak bc case with the friction coefficient, μ, equal to 0.5; Δ in the figures is the indenter penetration. The black curved line in the figures is the iso-strain contour for a strain of 0.1. The occurrence of the cutting mode of deformation with the $2\alpha = 30°$ wedge (Fig. 9(a)) and the radial-compression mode of deformation with the $2\alpha = 120°$ wedge (Fig. 9(c)) is quite clear. Furthermore, upon comparing the simulation results of Fig. 9 with the observations of the strain field and grid deformation summarized in Figs. 5 and 6, a close similarity is seen between the measurements and the simulation results with regard to all attributes of the bulk deformation. This is based on comparison of the strain patterns and magnitudes, locations of the high-strain zone 2 areas, grid deformation and intersection of the initially vertical grid lines with the indenter face. Only the wall layer of very high strain (zone 1) arising from friction effects, seen in Fig. 6 with the narrow-angle wedge, is not readily discernible. This could be due to an inability of the FE simulation to capture the wall strains due to the very high distortion of elements in this region. Or it could be a consequence of the weak bc which allows for material separation with minimal resistance. It would therefore be not unreasonable to conclude from these preliminary observations that the weak bc model is a good one for narrow-angle wedge indentation.

A more extensive, companion FE simulation study,[32)] carried out recently by one of us (NS), suggests that strong bc simulations (in an Arbitrary Lagrangian-Eulerian (ALE) framework) are able to more effectively capture the wall-layer of high strain seen with the narrow-angle wedge. However, with regard to the bulk deformation characteristics, the study found that the differences between the strong and weak bc simulation results were insignificant. This latter conclusion extended as well to load-penetration curves. It is envisaged that a study in progress — wedge-indentation experiments with 3–4 metals under lubricated and unlubricated conditions, concomitant with FE simulations employing both strong and weak bcs — will resolve any outstanding problems, including those concerning zones of intense strain-localization and wall-layers.

4.2 Other implications

The narrow-angle indentation framework, coupled with the direct observation and analysis approach, offers much scope for understanding indentation at a level that could lead to expanded application of indentation testing of material properties. This is in addition to the already-discussed possibility of studying friction under severe contact conditions, as in deformation processing, machining and other surface generation processes with metals. Some of these opportunities include exploration of strain gradient effects, development of ductile damage and failure models for metals, and fracture toughness testing. The strain-gradient probe is suggested by the highly localized strains generated by narrow angle wedge indentation. This localization and material "separation" seen in the experiments can also be a basis for exploring ductile failure, akin to notched specimens under

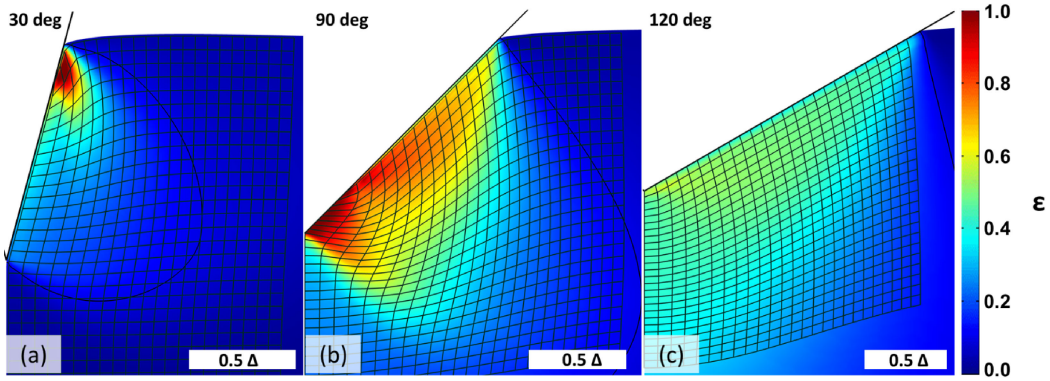

Fig. 9 Plastic strains obtained by FEA with weak bc for indentation with (a) 30°, (b) 90° and (c) 120° wedges. The curved black line in each panel is an iso-strain line with value 0.1.

tension; and for accentuating fracture at the indenter tip to explore fracture toughness measurements in metals. Further, the different spatial localizations of ε_p, shear and pressure using wedges of different 2α could be used to study phenomena like pressure-driven, phase-change in materials and microstructural changes. Due to close similarities between wedge and cone indentation, the weak b.c. approach should facilitate simulation of narrow-angle cone indentation. Lastly, the study of deformation near the tip of the narrow-angle wedge at higher-resolution may be of value for better understanding the material separation leading to chip formation in machining and other cutting processes.

5. Conclusions

A study has been made of the deformation patterns in wedge indentation of annealed metals. High-speed steel wedges with apex angles of 30°, 90°, and 120° are used to indent annealed OFHC Cu to a penetration depth of 1.5 to 2 mm. The material flow in the indentation zone is characterized by high-speed *in situ* imaging of material flow coupled with image correlation by Particle Image Velocimetry (PIV). Based on attributes of the deformation such as velocity and strain fields, and grid deformation, the deformation pattern is classified into two modes — a cutting mode with the narrow-angle, 30° indenter, and a radial-compression mode with the wide-angle, 120° indenter. It is shown that these attributes provide good signatures of the material flow and deformation modes. Material flow with the wide-angle indenters is found to be mostly normal to the indenter face, with negligible velocity component parallel to the indenter face. Consequently, friction at the indenter contact is unlikely to have any significant influence on the measured deformation response with wide-angle indenters. In contrast, with the narrow-angle indenters, there is significant material flow parallel to the indenter face. Hence, study of deformation fields, especially indenter wall layers, with narrow-angle indenters may offer much scope for understanding friction effects in metalworking contacts.

The results show that the challenges faced in modeling of narrow-angle indentation arise due to the prevailing cutting mode of deformation; they also point to how these may be overcome. Initial results from a successful simulation of narrow-angle indentation are discussed and found to be in good agreement with the *in situ* measurements of deformation. Various implications of the results for potentially new applications of (narrow-angle) indentation such as in tribology of metal forming and cutting processes, and assessment of ductile failure and damage in metals are briefly discussed.

Acknowledgements

This work was supported in part by NSF grants CMMI 1562470 and DMR 1610094 (AU and SC), and by JSPS KAKENHI Grant Number 18K13671 (TS). We should like to thank the anonymous referee for very insightful and constructive comments.

REFERENCES

1) D. Tabor: *The Hardness of Metals*, (Clarendon Press, Oxford, 1951).
2) H. O'Neill: *The Hardness of Metals and its Measurement*, 2nd ed., (Chapman and Hall, London, 1967).
3) W.C. Oliver and G.M. Pharr: J. Mater. Res. **7** (1992) 1564–1583.
4) R.F. Bishop, R. Hill and N.F. Mott: Proc. Phys. Soc. **57** (1945) 147.
5) R. Hill, E.H. Lee and S.J. Tupper: Proc. R. Soc. London, Ser. A **188** (1947) 273.
6) D.S. Dugdale: J. Mech. Phys. Solids **2** (1953) 14.
7) T.O. Mulhearn: J. Mech. Phys. Solids **7** (1959) 85.
8) J.B. Haddow: Int. J. Mech. Sci. **9** (1967) 159.
9) W. Hirst and M.G.J.W. Howse: Proc. R. Soc. London, Ser. A **311** (1969) 429.
10) K.L. Johnson: J. Mech. Phys. Solids **18** (1970) 115.
11) M.M. Chaudhri: Philos. Mag. Lett. **67** (1993) 107.
12) M.M. Chaudhri: Philos. Mag. A **74** (1996) 1213.
13) J.W. Kysar, Y.X. Gan, T.L. Morse, X. Chen and M.E. Jones: J. Mech. Phys. Solids **55** (2007) 1554.
14) T. Ohmura, A.M. Minor, E.A. Stach and J.W. Morris: J. Mater. Res. **19** (2004) 3626–3632.
15) J.A. Schey: *Tribology in Metal Working*, (American Society of Metals, OH, 1983).
16) N. Sundaram, Y. Guo and S. Chandrasekar: MRS Commun. **2** (2012) 47–50.
17) N. Sundaram, Y. Guo and S. Chandrasekar: Phys. Rev. Lett. **109** (2012) 106001.
18) Y. Guo, W.D. Compton and S. Chandrasekar: Proc. R. Soc. London, Ser. A **471** (2015) 20150194.
19) H. Yeung, K. Viswanathan, A. Udupa, A. Mahato and S. Chandrasekar: Phys. Rev. Appl. **8** (2017) 054044.
20) R.J. Adrian and J. Westerweel: *Particle Image Velocimetry*, (Cambridge University Press, Cambridge, 2011).
21) H. Yeung, K. Viswanathan, W.D. Compton and S. Chandrasekar: Proc. Natl. Acad. Sci. USA **112** (2015) 9828–9832.
22) M.C. Shaw: *Metal Cutting Principles*, (Oxford University Press, Oxford, 1984).
23) R. Hill: J. Mech. Phys. Solids **1** (1953) 265–270.
24) L.E. Samuels and T.O. Mulhearn: J. Mech. Phys. Solids **5** (1957) 125–134.
25) T. Sugihara, A. Udupa and K. Viswanathan: Mater. Trans. **60** (2019) https://doi.org/10.2320/matertrans.MD201907.
26) S. Biwa and B. Storåkers: J. Mech. Phys. Solids **43** (1995) 1303–1333.
27) A. Bhattacharya and W. Nix: Int. J. Solids Struct. **24** (1988) 881–891.
28) A. Giannakopoulos, P.L. Larsson and R. Vestergaard: Int. J. Solids Struct. **31** (1994) 2679–2708.
29) K. Jayadevan and R. Narasimhan: Comput. Struct. **57** (1995) 915–927.
30) M. Mata and J. Alcala: J. Mech. Phys. Solids **52** (2004) 145–165.
31) E. Hazell: Ph.D. thesis, University of Oxford, (2008).
32) N.K. Sundaram: Philosophical Magazine (2019) Under Review.